Available online at www.sciencedirect.com
SCIENCE DIRECT®
Journal of Computational Physics 189 (2003) 476–492
JOURNAL OF COMPUTATIONAL PHYSICS
www.elsevier.com/locate/jcp

New boundary constraints for elliptic systems used in grid generation problems

Upender K. Kaul

Computational Sciences Division, NASA Ames Research Center, Moffett Field, CA 94035, USA

Received 25 March 2002; received in revised form 8 April 2003; accepted 9 April 2003

Abstract

New boundary constraints for elliptic partial differential equations as used in grid generation problems in generalized curvilinear coordinate systems are proposed in this paper. These constraints, based on the principle of local conservation of thermal energy in the vicinity of the boundaries, are derived using the Green's Theorem. They uniquely determine the so called decay parameters in the inhomogeneous terms of these elliptic systems. These constraints [1] are designed for boundary clustered grids where large gradients in physical quantities need to be resolved adequately. It is observed that the present formulation also works satisfactorily for mild clustering. Therefore, a closure for the decay parameter specification for elliptic grid generation problems has been provided resulting in a fully automated elliptic grid generation technique. Thus, there is no need for a parametric study of these decay parameters since the new constraints fix them uniquely. It is also shown that for Neumann type boundary conditions, these boundary constraints uniquely determine the solution to the internal elliptic problem thus eliminating the nonuniqueness of the solution of an internal boundary value grid generation problem with Neumann boundary conditions.

Keywords: New boundary constraints; Automated elliptic grid generation; Decay parameters; Neumann boundary conditions; Conservation of thermal energy

1. Introduction

A large amount of effort has been devoted to developing, enhancing and using the grid generation capability (e.g., see [1–13]) through the solution of elliptic partial differential equations (pdes). As shown in the present study, elliptic pdes used in grid generation problems reduce to limiting forms near boundaries that are similar to the equations used in nuclear physics, diffusion–reaction problems, vortex problems, electric space charge problems, steady state heat transfer (conduction and convection) through long thin fins, etc. In the grid generation problems, these pdes contain appropriate inhomogeneous terms that control

E-mail address: kaul@email.arc.nasa.gov.
[1] Invention under US Patent application process.

0021-9991/$ - see front matter
doi:10.1016/S0021-9991(03)00229-8

the distribution of grid points especially near the boundaries. In the literature, the elliptic pdes used for grid generation are erroneously referred to as Poisson equations which contain source terms that are functions of only the independent variables, whereas, in the pdes for grid generation, these inhomogeneous terms also contain terms proportional to the dependent variables. Actually, in two-dimensional grid generation problems, close to a curvilinear boundary, the governing equations reduce to the long thin fin heat transfer equations with a finite heat transfer coefficient in the transverse direction (normal to the plane of paper) and a large heat transfer coefficient in the lateral direction.

Many of the elliptic grid generation studies referred to above have been centered on developing body conforming grids around bodies for external fluid flow simulations. The grids thus generated are smooth with at least first two derivatives continuous, appropriately stretched or clustered normal to any given coordinate direction and orthogonal over most of the grid domain. The inhomogeneous terms afford a grid control to satisfy clustering and orthogonality around specific surfaces (in three dimensions) and lines (in two dimensions).

In external flows, these inhomogeneous terms, i.e., the source terms and the dependent variable proportional terms, are designed to exponentially vanish away from the body so the problem reduces to solving a Laplacian away from the body.

In the present study, the inhomogeneous terms used are appropriate also for an interior grid generation problem where all the boundaries enveloping the grid will affect the solution through these terms. These terms are designed by interpreting their meaning physically through the principle of local conservation of thermal energy close to the grid boundaries.

The elliptic grid generation methodology used here has been shown to work for numerous geometrical configurations in [1,2,4] and a host of other applications in other reported studies. The important improvement in the present study over these previous methods is in the provision of the new set of boundary constraints that obviates the need for time-consuming manual hit and trial decay parameter specification. Additionally, these decay parameters have been defined as functions of appropriate coordinate variables along a given boundary and are not just constants along that boundary, which makes it possible to automatically cluster the grids in two orthogonal directions in the vicinity of two adjacent boundaries. The new constraints are applicable to both two-dimensional and three-dimensional grid generation problems.

The problems of grid cross-over resulting in negative Jacobians are eliminated since the energy conservation is satisfied all over the domain. The elliptic pdes are solved without any free parameters making the procedure fully automatic. There is no need for any intermediate transformation and redistribution of points along boundaries, as in, e.g. [10]. Also, there is no need for prescription of the grid cell aspect ratio (the distortion function, $f(\xi,\eta)$), as in [11] or for the prescription of distributed force functions which involve another free parameter, a force constant, as in [12]. Also, unlike in [13], where the Neumann–Dirichlet boundary conditions cannot be used when distortion function is calculated iteratively from its definition equation, any combination of Neumann–Dirichlet boundary conditions can be used in the present method.

However, having said that, for certain boundary point distributions along the boundaries, strictly orthogonal grid near those boundaries may not be attained, as is the case in other methods too. In studies [10–13] reported earlier, the distinction has been made between the strictly orthogonal and the nearly orthogonal grids, which correspond to strong and weak constraint formulations, respectively, as discussed in an earlier study [11]. For example, Visbal and Knight [10] state that the strictly orthogonal grids can be generated with a partial control of the mesh spacing and nearly orthogonal grid with strict control of the mesh spacing. This is in keeping with the observation that with Neumann boundary conditions, the grids generated near the boundaries are strictly orthogonal at those boundaries, but only nearly orthogonal with Dirichlet boundary conditions prescribed at those boundaries.

Various geometrical configurations, an annulus, a square, a convex geometry used as a test case in [11–13], a gear-tooth and a full gear are considered to demonstrate the usefulness of the new boundary constraints derived in this study. The gear tooth geometry treated here corresponds to that of a planar

cross-section of a spiral-bevel pinion gear tooth typical of the OH-58 helicopter transmission pinion. This study is driven by the need to generate time-series vibration signatures from the OH-58 helicopter transmission by finite-difference simulation using the appropriate structural dynamic equations. The choice of elliptic pdes for grid generation is entailed by the need to generate time series data as accurately as possible (see relative comparison with other representative grid generation methods in [9]).

2. Governing equations

The derivation of the boundary constraints as applied to two-dimensional grid generation problems is given below. The extension to three dimensions is straightforward, and results of a three-dimensional study using the new constraints will be reported later.

The two-dimensional governing equations for an elliptic grid generation problem in an appropriately defined planar domain, as given in [1,2], are

$$\xi_{xx} + \xi_{yy} = P(\xi, \eta),$$

$$\eta_{xx} + \eta_{yy} = Q(\xi, \eta),$$

where ξ and η are the generalized curvilinear coordinates, x and y are the Cartesian coordinates, and the $P(\xi, \eta)$ and $Q(\xi, \eta)$ are the inhomogeneous terms.

The form of the inhomogeneous terms, P and Q, as proposed by Thompson et al. [2] is exponential and is given by

$$P(\xi, \eta) = -a_i \operatorname{sgn}(\xi - \xi_i) \exp(-b_i|\xi - \xi_i|),$$

$$Q(\xi, \eta) = -c_i \operatorname{sgn}(\eta - \eta_i) \exp(-d_i|\eta - \eta_i|),$$

where the suffix i refers to the grid boundary in question, b_i and d_i are specified constants, called the decay parameters, and a_i and b_i are also specified constants, where $a_i = c_i$ and $b_i = d_i$.

Steger and Sorenson [4] modified these terms to control the grid close to a given coordinate boundary, say, η, as

$$P(\xi, \eta) = -a_i(\xi) \operatorname{sgn}(\eta - \eta_i) \exp(-b_i|\eta - \eta_i|),$$

$$Q(\xi, \eta) = -c_i(\xi) \operatorname{sgn}(\eta - \eta_i) \exp(-d_i|\eta - \eta_i|),$$

where $a_i(\xi)$ and $c_i(\xi)$ are calculated iteratively as part of the solution to satisfy both the orthogonality condition at a given boundary η_i as well as the requirement of a given spacing at that boundary.

In the present study, these terms are further modified as a set for each coordinate direction as

$$P(\xi, \eta) = -a_i(\xi) \operatorname{sgn}(\eta - \eta_i) \exp(-b_i(\xi)|\eta - \eta_i|), \tag{1a}$$

$$Q(\xi, \eta) = -c_i(\xi) \operatorname{sgn}(\eta - \eta_i) \exp(-d_i(\xi)|\eta - \eta_i|) \tag{1b}$$

for a given η_i boundary, and

$$P(\xi, \eta) = -e_i(\eta) \operatorname{sgn}(\xi - \xi_i) \exp(-f_i(\eta)|\xi - \xi_i|), \tag{1c}$$

$$Q(\xi, \eta) = -g_i(\eta) \operatorname{sgn}(\xi - \xi_i) \exp(-h_i(\eta)|\xi - \xi_i|) \tag{1d}$$

for a given ξ_i boundary, where the decay parameters, $b_i(\xi) = d_i(\xi)$ and $f_i(\eta) = h_i(\eta)$ are now defined as functions of the appropriate coordinate variables. As shown below, choice of parameters, $b_i = d_i$ and $f_i = h_i$ is appropriate, based on the physical analogies derived from the limiting form of Eqs. (1a), (1b) and Eqs. (1c), (1d), respectively.

Now, for the sake of argument, without loss of generality, if we take the case where $\xi > \xi_i$ and $\eta > \eta_i$, then we have the two sets of inhomogeneous terms as

$$P(\xi,\eta) = -a_i(\xi)\exp(-b_i(\xi)(\eta-\eta_i)), \tag{1e}$$

$$Q(\xi,\eta) = -c_i(\xi)\exp(-b_i(\xi)(\eta-\eta_i)) \tag{1f}$$

for a given η_i boundary, and

$$P(\xi,\eta) = -e_i(\eta)\exp(-f_i(\eta)(\xi-\xi_i)), \tag{1g}$$

$$Q(\xi,\eta) = -g_i(\eta)\exp(-f_i(\eta)(\xi-\xi_i)) \tag{1h}$$

for a given ξ_i boundary.

At the boundaries, where $\xi = \xi_i$ and $\eta = \eta_i$, Eqs. (1e)–(1h), respectively, become

$$P(\xi,\eta) = -a_i(\xi),$$

$$Q(\xi,\eta) = -c_i(\xi)$$

for a given η_i boundary, and

$$P(\xi,\eta) = -e_i(\eta),$$

$$Q(\xi,\eta) = -g_i(\eta)$$

for a given ξ_i boundary.

Consider a given η_i boundary. When $b_i(\xi)(\eta-\eta_i)$ is small, the inhomogeneous terms take the form given by

$$P(\xi,\eta) = -a_i(\xi)(1-b_i(\xi)(\eta-\eta_i))$$

and

$$Q(\xi,\eta) = -c_i(\xi)(1-b_i(\xi)(\eta-\eta_i)).$$

Similarly, consider a given ξ_i boundary. When $f_i(\eta)(\xi-\xi_i)$ is small, the inhomogeneous terms take the form given by

$$P(\xi,\eta) = -e_i(\eta)(1-f_i(\eta)(\xi-\xi_i))$$

and

$$Q(\xi,\eta) = -g_i(\eta)(1-f_i(\eta)(\xi-\xi_i)).$$

Therefore, the governing equation for, e.g., ξ, in the vicinity of the boundary ξ_i, becomes

$$\xi_{xx} + \xi_{yy} = -e_i(\eta)(1-f_i(\eta)(\xi-\xi_i))$$

or

$$\xi_{xx} + \xi_{yy} - e_i(\eta)f_i(\eta)\xi = -e_i(\eta) - e_i(\eta)f_i(\eta)\xi_i. \tag{2}$$

If the term, $e_i f_i \xi$, were absent, the resulting equation would turn out to be a Poisson equation. The equation given above arises, e.g., in the steady state heat conduction problems in long thin fins, where ξ is the temperature and where the heat transfer coefficient in the transverse thin direction is moderate but is large in the lateral direction, and there is a balance amongst the heat conducted through the fin, heat carried away from or to it through convection in proportion to this moderate heat transfer coefficient and the heat sources/sinks distributed over the domain. Consider the case when $\xi > \xi_i$, then, defining a new variable

$$\theta = \xi - \xi_i.$$

Eq. (2) becomes

$$\theta_{xx} + \theta_{yy} - e_i(\eta) f_i(\eta) \theta = -e_i(\eta). \tag{3}$$

The term, $-e_i$, can be interpreted as a heat source term.

Eq. (3) tells us that when $\xi > \xi_i$, there is a balance among the heat conducted from a control volume in the interior to the boundary ξ_i, heat convected out of this control volume and the heat generated within the control volume due to the heat source, $e_i(\eta)$.

Similarly, if we consider the case when $\xi_i > \xi$, then Eq. (2) becomes

$$\theta_{xx} + \theta_{yy} - e_i(\eta) f_i(\eta) \theta = e_i(\eta), \tag{4}$$

where $\theta = \xi_i - \xi$.

The term, $e_i(\eta)$, can be interpreted as a heat sink term.

Again, Eq. (4) tells us that when $\xi < \xi_i$, there is a balance among the heat convected from the boundary ξ_i to a control volume in the interior, heat conducted into the control volume and the heat lost from the control volume due to the sink, $e_i(\eta)$.

From Eqs. (3) and (4), it can be seen that for a given convective heat flux (given number of grid lines), as the product, $e_i f_i$, decreases, the heat transfer coefficient decreases proportionally in magnitude which means that the temperature gradient at the boundary ξ_i has increased so that ξ approaches ξ_i rapidly near the boundary. This means that there is a large gradient in ξ from the grid boundary i to the interior, thereby resulting in a highly clustered grid near the boundary.

Away from this grid boundary, $f_i(\eta)|\xi - \xi_i|$ is large, and $P(\xi, \eta) \to 0$, $Q(\xi, \eta) \to 0$ (from Eqs. (1c) and (1d)); therefore, we are left with the Laplace equation, $\Delta\xi = 0$. Extremum principle is unconditionally maintained there, since the solution is harmonic in this case.

Similar arguments hold for a given η_i boundary.

Referring to Eqs. (3) and (4), for a given boundary, ξ_i, the Green's Theorem gives us, respectively,

$$\int\int_S (-e_i(\eta) + e_i(\eta) f_i(\eta) \theta)\, \mathrm{d}\sigma = \int_C \partial_n \theta \, \mathrm{d}s, \tag{5}$$

$$\int\int_S (e_i(\eta) + e_i(\eta) f_i(\eta) \theta)\, \mathrm{d}\sigma = \int_C \partial_n \theta \, \mathrm{d}s, \tag{6}$$

where S is the surface area of a closed domain, C is the boundary enclosing this domain, n is the normal to the boundary, $\mathrm{d}\sigma$ is the elemental area and $\mathrm{d}s$ is an elemental arc.

The integrands on the left-hand side, $\pm e_i(\eta)$ and $e_i(\eta) f_i(\eta) \theta$ represent the heat sink/source term and the convection term respectively, and the integrand on the right-hand side represents the heat flux through the boundary C.

Eqs. (5) and (6) are used as constraints to fix $f_i(\eta)$ uniquely for a solution consistent with the specification of the boundary data. The extremum principle will be satisfied at the ith boundary, which is the requirement in the grid generation problems, since the energy conservation principle is satisfied. The term,

$\pm e_i(\eta)$, respectively in Eqs. (6) and (5), is calculated iteratively through the solution process, as in [4], which together with $f_i(\eta)$ ensures the grid orthogonality and a given grid spacing at the ith grid boundary.

In the design of the inhomogeneous terms, $P(\xi,\eta)$ and $Q(\xi,\eta)$ in e.g., Eqs. (1c) and (1d), there is no restriction on the nature of the sink/source term, $\pm e_i(\eta)$. It can change sign which indicates the presence of sources and sinks, subject to the constraint given by Eqs. (5) and (6). Otherwise, improper combinations of sources and sinks will violate the extremum principle. If over the domain, there is a net rate of heat generation due to the source/sink combination, then there has to be a positive heat flux convected away and vice versa. This requirement will automatically be satisfied by Eqs. (5) and (6).

If there is a point heat source present in the domain, the isothermals (temperature, i.e., ξ or η, contour lines) will tend to cluster around it since the gradients in the vicinity of the source will be positive toward the source and high, depending upon the strength of the source, and conversely for a heat sink. Same argument applies to a line heat source and sink. By analogy, if the source term turns out to be positive over some parts of the domain, then the curvilinear coordinate lines will tend towards lines with higher coordinate values and vice versa.

It may be noted here that the orthogonality and boundary spacing constraints of [4] are coupled with the new boundary constraints (Eqs. (5) and (6). The present approach removes the conflict between the parameters, e_i and f_i, through, e.g., Eq. (4), since the rate of clustering is determined by the product of e_i and f_i, and not by f_i alone. Previously, without the availability of, e.g., Eq. (4), the value of e_i that would be calculated through the method of [4], would turn out to be different from the one calculated in the present case since e_i has to satisfy the constraint posed by Eq. (4).

Again, it is worth noting here that the decay parameter, e.g., $f_i(\eta)$, is defined as a function of a given coordinate direction, η, along a given ξ boundary, and the boundary constraints, Eqs. (5) and (6), are applied piece-meal along that ξ boundary by considering a series of small control volumes along that boundary. This approach lends itself to a very quick and explicit calculation of the decay parameter function from the boundary constraints, since the constraints are not transcendental, once $e_i(\eta)$ is calculated. As for clustering at various given locations in a given coordinate direction, the boundary constraints need to be applied over a small extent of that coordinate direction, i.e., over a small control volume, and the control volume can be made arbitrarily small by the appropriate initial prescription of grid points along that boundary.

Similarly, for a given boundary, η_i, the corresponding constraints are

$$\int\int_S (-c_i(\xi) + c_i(\xi) b_i(\xi)\theta)\,\mathrm{d}\sigma = \int_C \partial_n\theta\,\mathrm{d}s, \tag{7}$$

$$\int\int_S (c_i(\xi) + c_i(\xi) b_i(\xi)\theta)\,\mathrm{d}\sigma = \int_C \partial_n\theta\,\mathrm{d}s. \tag{8}$$

3. Solution procedure

First, the boundary data are selected appropriate to the physics of the problem, so that the gradients in physical quantities can be resolved adequately. Since there is a symmetry plane and a rotational symmetry present in the gear problem, the half-tooth grid is reflected about this symmetry plane and then the tooth grid is rotated about a moving axis of periodicity, thus substantially reducing the computational effort in prescribing the initial distribution of the entire 19-tooth gear at time, $t = 0$. But, for the elliptic grid generation of the entire gear after this initial time, periodic boundary conditions are used in the circumferential direction in the interior. Dirichlet boundary conditions are prescribed along the circumferential direction on the inner and outer boundaries. Same set of boundary conditions are used for the grids for an annulus.

For the grids for the square and the convex geometries, Dirichlet boundary conditions are prescribed along two opposing boundaries in one coordinate direction, ξ, and Neumann boundary conditions are prescribed along the other two opposing boundaries in the other coordinate direction, η, i.e., Dirichlet along the upper and lower boundaries and Neumann along the left and right boundaries.

Then, by interchanging the independent and dependent variables, the governing equations to be solved in the computational space (ξ, η) become

$$\alpha x_{\xi\xi} - 2\beta x_{\xi\eta} + \gamma x_{\eta\eta} = -J^2(P(\xi,\eta)x_\xi + Q(\xi,\eta)x_\eta),$$

$$\alpha y_{\xi\xi} - 2\beta y_{\xi\eta} + \gamma y_{\eta\eta} = -J^2(P(\xi,\eta)y_\xi + Q(\xi,\eta)y_\eta).$$

These equations are solved in the computational space using a line SOR relaxation algorithm where each coordinate line in one curvilinear coordinate direction is solved semi-implicitly using the Thomas algorithm for tri-diagonal systems. The inhomogeneous terms referred to above are designed and incorporated so that a desired grid behavior near the boundaries is achieved.

The inhomogeneous problem is solved using a technique similar to that of [4] by over-relaxing the inhomogeneous terms during the iteration process. The inhomogeneous terms used in [4] are well suited for external boundary value problems where clustering is allowed in only one curvilinear coordinate direction, normal to the body. But, in internal boundary value problems, inhomogeneous terms have to take account the influence of the boundaries in both curvilinear coordinate directions. As discussed above, the inhomogeneous terms used here allow for clustering in both coordinate directions automatically.

The inhomogeneous terms, $P(\xi,\eta)$ and $Q(\xi,\eta)$, are evaluated at the boundaries in terms of the left-hand side at each line relaxation sweep. Then away from each boundary, the inhomogeneous terms are attenuated through an exponential function in each direction, as discussed above. In ξ direction, this exponential term is of the form, $-e_i(\eta)\exp(-f_i(\eta)|\xi - \xi_i|)$, for $P(\xi,\eta)$ and of the form, $-g_i(\eta)\exp(-f_i(\eta)|\xi - \xi_i|)$ for $Q(\xi,\eta)$.

In what is stated above, a proof of concept study for an annulus, a square, a convex geometry and a gear-tooth is carried out to demonstrate the usefulness of the new boundary constraints. Then, the grid for a complete 19-tooth gear is generated using periodic boundary conditions in the circumferential direction. This is the only way to solve the grid generation problem in a larger context of structural dynamical simulation of the gear, since the grid for the entire gear will be subjected to dynamic stresses nonuniformly.

The boundary constraints given by, e.g., Eqs. (7) and (8), are applied to a region close to the boundary. For example, a finite slender strip close to the boundary, $\eta_{\max}$, as shown in Fig. 1, is used as a control

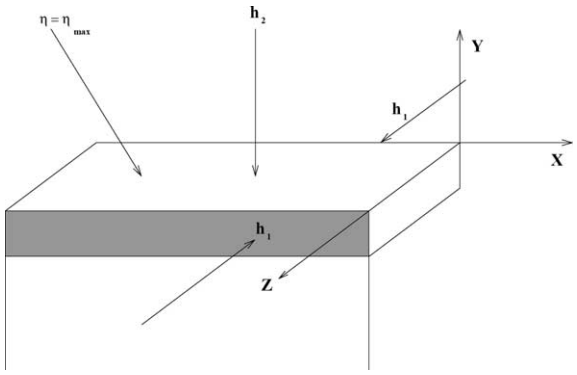

Fig. 1. A schematic showing the finite slender strip over which the boundary constraint is applied; pin is thin in the z-direction.

volume to evaluate the heat sink term and the convective flux term over it with the net heat flux calculated around it. At the $\eta = \eta_{max}$ boundary, the heat transfer coefficient, h_2 is large, whereas the heat transfer coefficient, h_1 is moderate. The pin fin is thin in the z direction, and the ambient enveloping the fin in the neighborhood of and around the η_{max} boundary can be imagined to be at a temperature, $\eta_\infty = \eta_{max}$, since h_2 is large. Now, as h_1 becomes smaller, the temperature gradient in the y direction near the boundary η_{max} increases, for a given heat flux (given number of grid lines, per the boundary prescription), and therefore the clustering there becomes denser. This is the physical basis for the argument that the clustering at a given boundary becomes denser when the decay parameter, e.g., $b_i(\xi)$, associated with the $c_i b_i \theta$ term in Eq. (7) decreases.

However, the caveat here is that the thin fin analogy holds for a two-dimensional case only. The boundary constraints are easily extended to three dimensions, but the physical analog is not now a thin fin. The results of a study discussing three-dimensional version of the new constraints will appear later.

4. Results

The new boundary constraints have been validated by generating two-dimensional interior grids for an annulus, a square, a convex geometry, a gear-tooth and a complete gear. Fig. 2 shows an interior grid for an annulus, clustered at two opposing η boundaries. The degree of clustering at/near the η boundaries is measured by a clustering parameter, $\Delta S/\Delta S_{av}$, where ΔS is the normal spacing at the η boundary and ΔS_{av} is the average spacing based on the length of the ξ coordinate line from one η boundary to the opposing η boundary and the number of grid points along this ξ coordinate line. Therefore, as the clustering parameter at a given boundary decreases in value, clustering becomes denser at/near that boundary and vice versa.

Figs. 3(a) and (b) show the distribution of the lower and upper boundary decay parameter functions over the circumference corresponding to the clustering parameter value of 0.1, and Figs. 3(c) and (d) show the convergence history of an averaged decay parameter value (averaged over the circumference) for both the lower and upper boundaries. Calculations are stopped when the relative convergence criterion that the final average spacing at any given boundary be within 10% of the initial average spacing at that boundary is met.

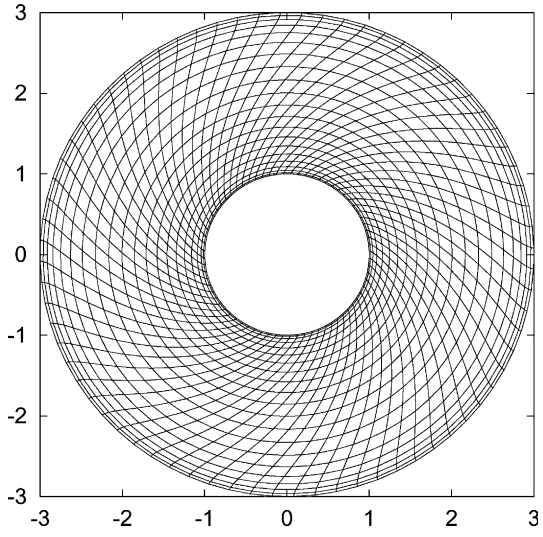

Fig. 2. Finite difference grid of annulus, clustering parameter = 0.1.

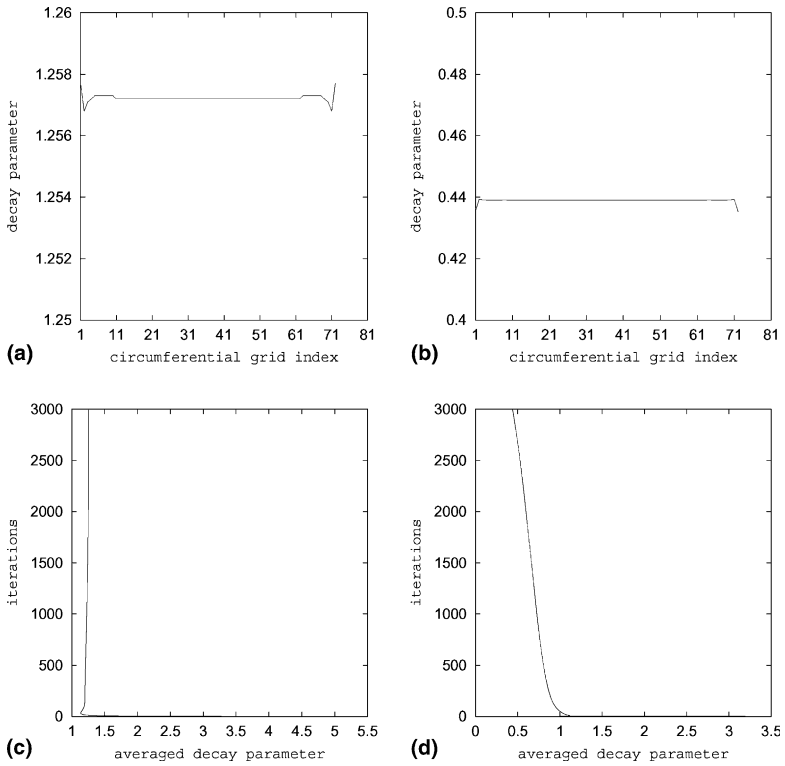

Fig. 3. Results for the annulus: lower boundaries (a,c) and upper boundaries (b,d). (a) and (b) decay parameter function distribution over the circumference; (c) and (d) convergence history of decay parameter averaged over the circumferential direction.

As is seen in Figs. 3(a) and (b), the decay parameter function is uniform in the circumferential direction, as expected in the case of the annulus, except for the end effects due to a different discretization stencil at the end points (periodic boundary conditions). In Figs. 3(c) and (d), the decay parameter averaged over the circumferential direction is seen to rapidly converge to steady state values of 1.26 and 0.44 for the lower and upper boundaries, respectively (see Table 1). Corresponding to this converged solution, the decay functions that attenuate the inhomogeneous terms for the lower and upper boundaries are shown in Figs. 4(a) and (b). The ordinate in these figures shows the number of grid points along a given ξ coordinate line between

Table 1
Grid characteristics

Grid	Clustering parameters		Averaged decay parameter			
	ξ	η	Lower	Upper	Left	Right
Annulus		0.1	1.26	0.44		
Annulus		0.5	1.22	0.74		
Square	5.0	0.1	0.81			0.58
Square	5.0	5.0		0.57		0.54
Convex		6.0		0.39		
Convex		5.0		0.45		
Convex		3.0		0.52		
Gear		0.1	0.93	0.55		
Gear		5.0		0.59		

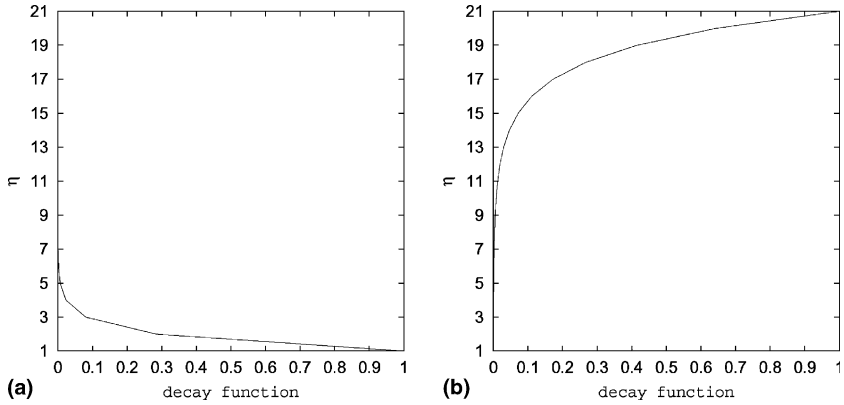

Fig. 4. Results for the annulus: lower boundary (a) and upper boundary (b). (a) and (b) Distribution of the decay function (based on the circumferentially averaged decay parameter, $b_{i_{av}}$), $\exp(-b_{i_{av}}|\eta - \eta_i|)$, along the radial-like η coordinate.

the top and bottom η boundaries, and the abscissa represents the decay function based on the circumferentially averaged decay parameter.

For comparison, Fig. 5 shows the grid for the annulus with a clustering parameter of 0.5. As is shown in Table 1, the averaged decay parameter value at the upper η boundary increases to 0.74, as expected, but does not change appreciably at the lower η boundary. The reason for this is that the upper boundary does not now attract as many η grid lines toward it as before when the clustering parameter of 0.1 was used. Hence, more η grid lines are pushed toward the lower η boundary, thus keeping the lower boundary decay parameter from increasing proportionately.

A more rigorous test case of an internal grid in a square is considered in Figs. 6–8. The grid is clustered in both the coordinate directions, ξ and η. The decay parameter functions in both coordinate directions are calculated simultaneously as part of the solution. Fig. 6 shows the converged grid clustered in both horizontal and vertical directions. The clustering is achieved according to the clustering parameter of 0.1 in the vertical direction from lower boundary to the upper boundary and clustering parameter of 5.0 in the

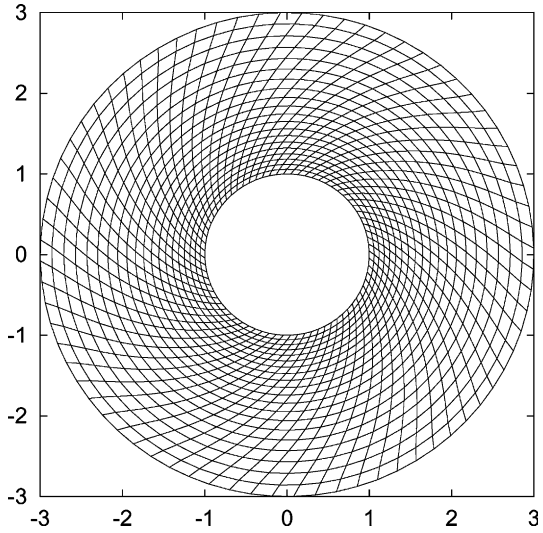

Fig. 5. Finite difference grid of annulus, clustering parameter = 0.5.

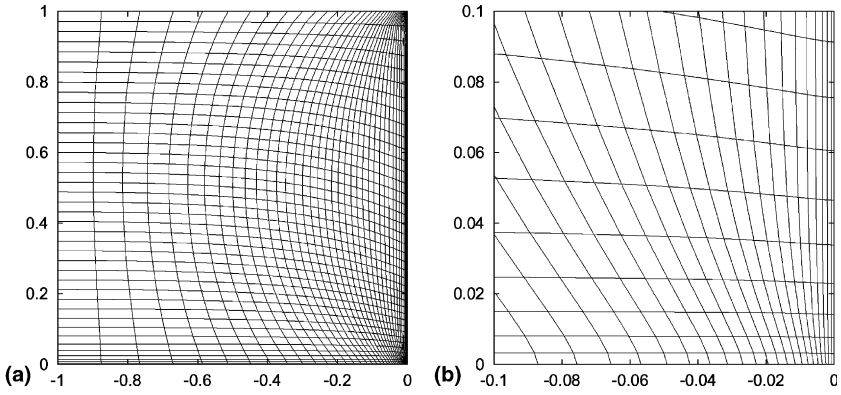

Fig. 6. Finite difference grid of square, ξ clustering parameter = 5.0, η clustering parameter of 0.1. (a) Complete square. (b) Enlarged view of lower right corner.

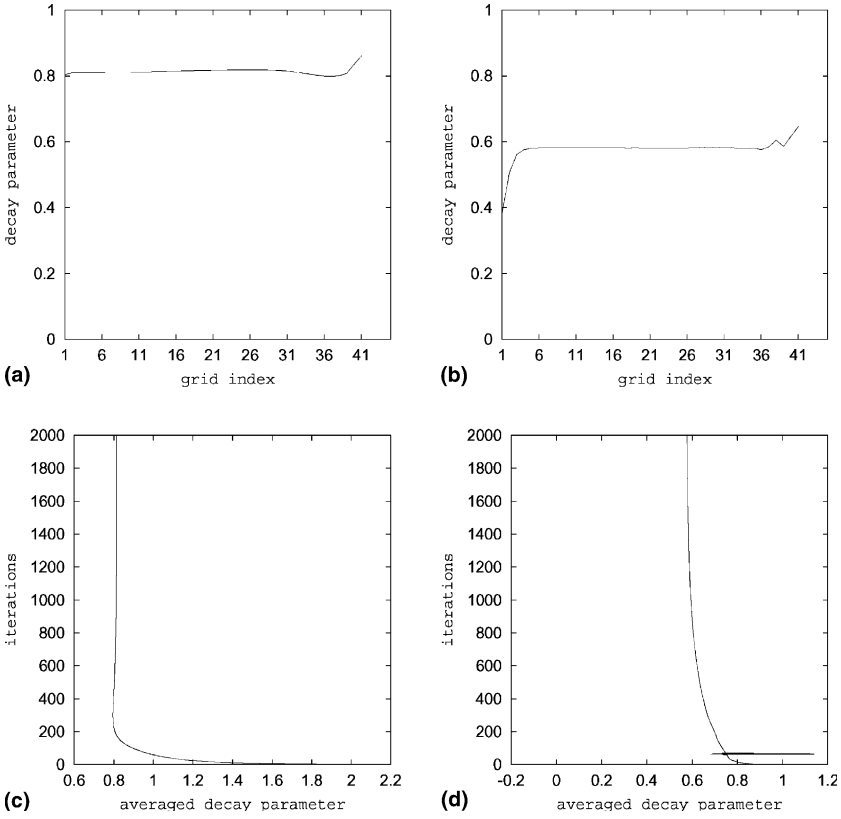

Fig. 7. Results for the square: lower boundaries (a,c) and right boundaries (b,d). (a) and (b) distribution of decay parameter function over the corresponding boundaries; (c) and (d) convergence history of decay parameter function averaged over the corresponding boundaries.

horizontal direction from the left to the right boundary. Clustering parameter of 5.0 in the ξ direction ensures the coarsest grid at the left boundary. At the left and right boundaries, Neumann boundary conditions are applied and Dirichlet boundary conditions are specified over the lower and upper boundaries. As stated above, nearly orthogonal grid is realized at the lower and upper boundaries. But, strictly

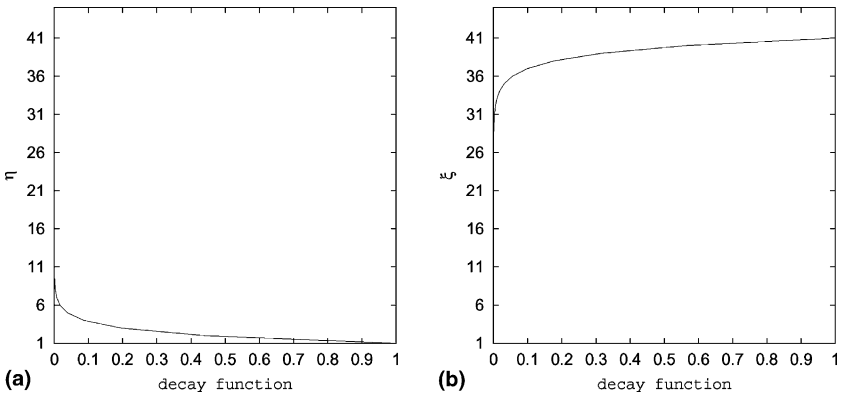

Fig. 8. Results for the square: distribution of the decay function (based on appropriately averaged decay parameter). (a) Lower boundary $\exp(-b_{i_{av}}|\eta - \eta_1|)$. (b) Right boundary, $\exp(-f_{i_{av}}|\xi - \xi_{max}|)$.

orthogonal grid at the left and right boundaries is realized because the initial prescription of grid points on the left and right boundaries is overridden by the Neumann boundary conditions thus allowing the grid points at these boundaries to float to ensure strict orthogonality there.

Figs. 7(a) and (b) show the distribution of the respective decay parameter functions along the lower (η_1) and right (ξ_{max}) boundaries.

Figs. 7(c) and (d) show average decay parameter (averaged over the corresponding coordinate boundary) convergence history (see Table 1 for the values for corresponding averaged decay parameters).

Corresponding to this converged solution, the decay functions that attenuate the inhomogeneous terms for the lower and right boundaries are shown in Figs. 8(a) and (b). The ordinate in these figures shows the number of grid points along a given coordinate line between the two orthogonal opposing boundaries, and the abscissa represents the decay function appropriately averaged along a given boundary.

Again, for comparison, Fig. 9 shows the grid for the square with clustering parameter of 5.0 for both the ξ and η directions. Corresponding values of the averaged decay parameter are shown in Table 1.

In Fig. 10, a grid for the convex geometry corresponding to a clustering parameter of 6.0 was generated. The convex geometry (see e.g. [13]) is defined as follows

$$x = -1, \quad x = 0, \quad y = 0, \quad y = 0.75 + 0.25\sin(\pi(0.5 - 2x)).$$

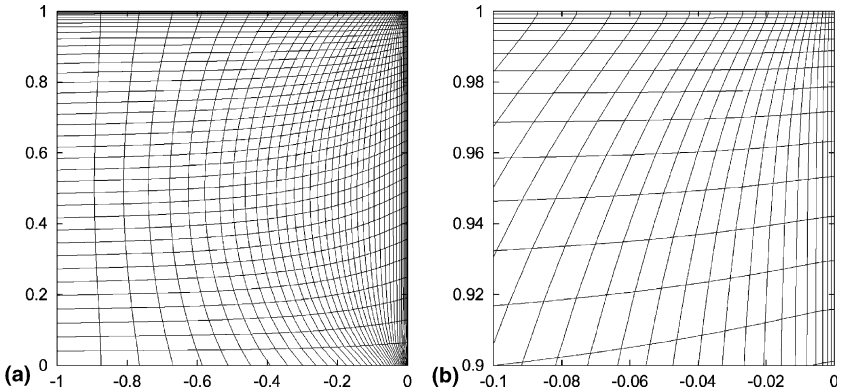

Fig. 9. Finite difference grid of square, ξ clustering parameter = 5.0, η clustering parameter = 5.0. (a) Complete square. (b) Enlarged view of upper right corner.

Grid is clustered at the upper boundary (η_{max}), corresponding to a clustering parameter 6.0 at the lower boundary to ensure the coarsest grid at the lower boundary and the finest at the upper boundary. At the left and right boundaries, Neumann boundary conditions are applied and Dirichlet boundary conditions are specified over the lower and upper boundaries. As in the case of a square (Figs. 6 and 9), nearly orthogonal grid is realized at the lower and upper boundaries. Again, strictly orthogonal grid at the left and right boundaries is realized due to the application of the Neumann boundary conditions there.

Figs. 10–12 show the grids for the convex geometry corresponding to clustering parameters of 6.0, 5.0 and 3.0. As is shown in Table 1, the corresponding values for the averaged decay parameter increase from 0.39 to 0.45 to 0.52 as the clustering parameter decreases from 6.0 to 5.0 to 3.0. This clearly establishes the inverse relationship as postulated in the Governing Equations section, namely, the lower the decay pa-

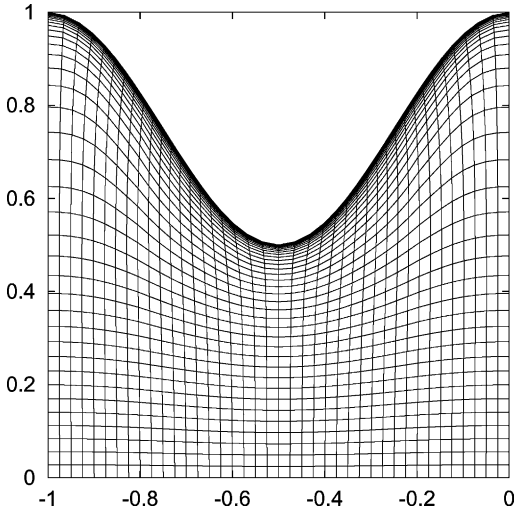

Fig. 10. Finite difference grid of the convex geometry, clustering parameter = 6.0.

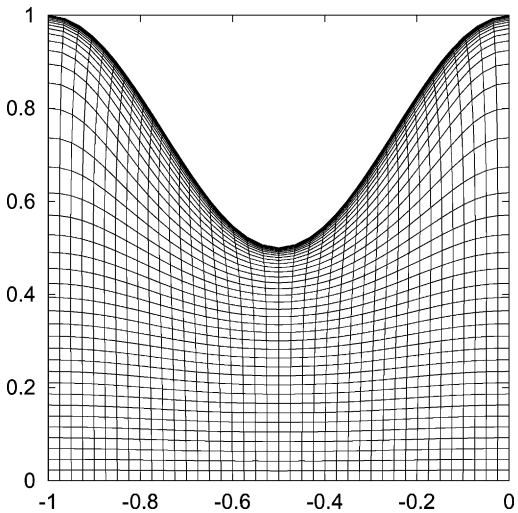

Fig. 11. Finite difference grid of the convex geometry, clustering parameter = 5.0.

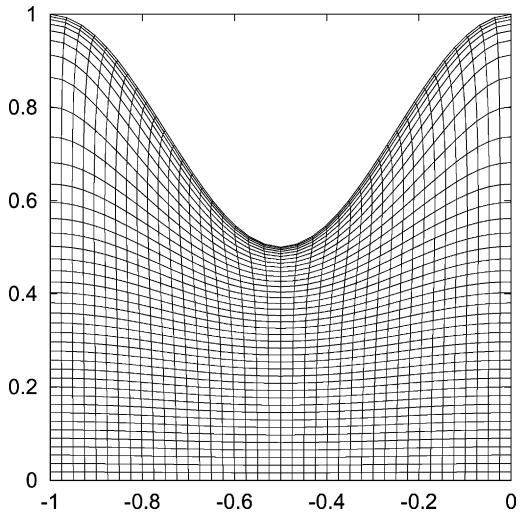

Fig. 12. Finite difference grid of the convex geometry, clustering parameter = 3.0.

rameter at a given boundary, the higher the clustering at that boundary. Stated differently, lower the decay parameter at a given boundary, the lower the clustering parameter associated with that boundary, or higher the clustering parameter associated with the opposite boundary.

Corresponding decay function attenuation rates are shown in Figs. 13(a)–(c). It is observed that the decay function decays from a value of 1.0 to 1.e − 03 within 18 grid points from the $\eta_{\max}$ boundary corresponding to Fig. 10, within 15 points corresponding to Fig. 11 and within 9 points corresponding to Fig. 12. This is consistent with the fact that the higher the clustering rate, the more spread out the decay function is away from the boundary.

Hence, the rapidity with which the decay function gets attenuated is a function of the clustering parameter. The lower the clustering parameter specific to a given boundary, the smaller the decay parameter corresponding to that boundary, the more clustered the grid is at that boundary and, therefore, the lower the rapidity with which the decay function gets attenuated away from that boundary.

In the convex geometry example, clustering parameters of 3.0, 5.0 and 6.0 were selected to show that the underlying assumptions for the boundary constraints work well even for mild to moderate clustering parameters or that they work well even for decay parameters of the order of 1 (i.e., 0.52, 0.45, 0.39, respectively). This is important since the extent of applicability of the proposed boundary constraints is thus demonstrated to be large. Obviously, for even smaller decay parameters (less than order of 1), for which the

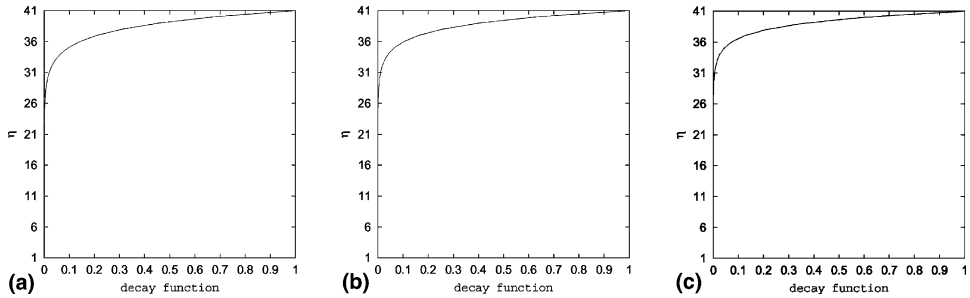

Fig. 13. Results for the convex geometry: (a)–(c) Decay function (based on $b_{i_{\text{av}}}$), $\exp(-b_{i_{\text{av}}}|\eta - \eta_{\max}|)$. Clustering parameters: (a) 6.0; (b) 5.0; (c) 3.0.

underlying assumptions tend towards being rigorously valid, the boundary constraints are even more applicable.

Fig. 14 shows the gear tooth grid for one-sided clustering at the η_{max} (upper) boundary. The value of the clustering parameter at the lower boundary is 5.0, which means that the grid is coarsest at the lower boundary and it progressively gets refined toward the upper boundary. Dirichlet boundary conditions were applied at the ξ_1 (left) and ξ_{max} (right) boundaries.

As a comparative example, a test case was run with an a priori prescribed value of the decay parameter of 0.15 corresponding to the case shown in Fig. 14, i.e., with a clustering parameter value of 5.0, and the resulting grid rapidly degrades as shown in Fig. 15(a), and the corresponding solution convergence history is shown in Fig. 15(b), where after 50 iterations, the solution aborts due to negative values of Jacobians.

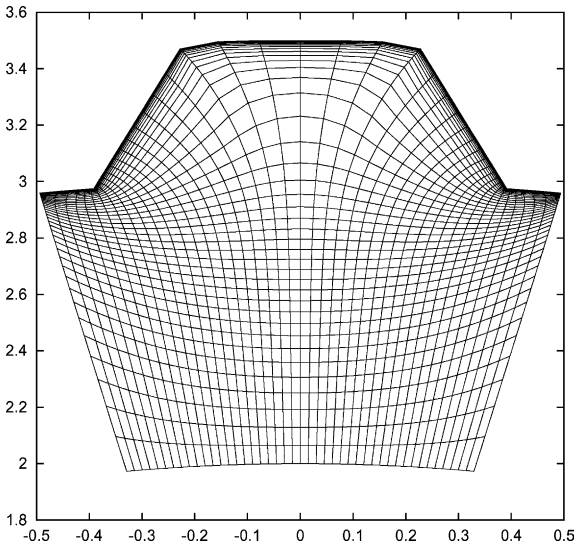

Fig. 14. Finite difference grid of pinion gear tooth, clustering parameter = 5.0.

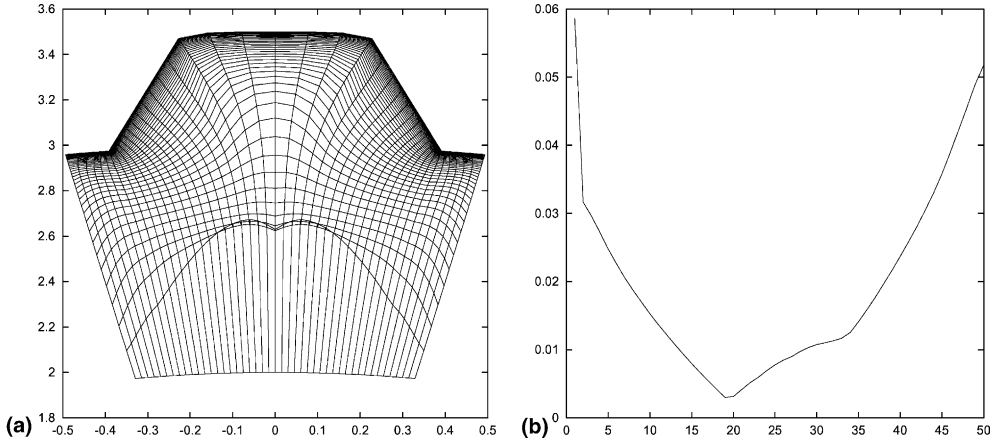

Fig. 15. Comparative results for the gear tooth with a fixed decay parameter value of 0.15; clustering parameter of 5.0: (a) grid for the tooth (negative Jacobians); (b) convergence history (solution diverges rapidly in 50 iterations).

This is just an example of the problems encountered in the trial-and-error process in prescribing the decay parameter manually, for which now a solution has been found through the new constraints derived in the present study.

Fig. 16 shows a section of the complete 19-tooth gear grid which was generated using periodic boundary conditions in the ξ direction (circumferential direction) with a clustering parameter of 0.1.

The resulting grid is smooth and orthogonal throughout in this case, as expected. The strict enforcement of orthogonality at the ξ boundaries is ensured here since the grid for the 19-tooth gear is generated with the periodic boundary conditions prescribed at these boundaries.

Another grid simulation with the clustering parameter value of 5.0 was made with the complete 19-tooth gear. The corresponding grid is shown in Fig. 17.

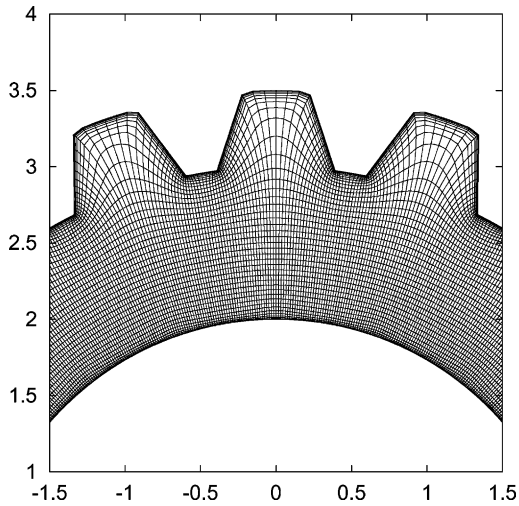

Fig. 16. Section of a finite difference grid of pinion gear, clustering parameter = 0.1.

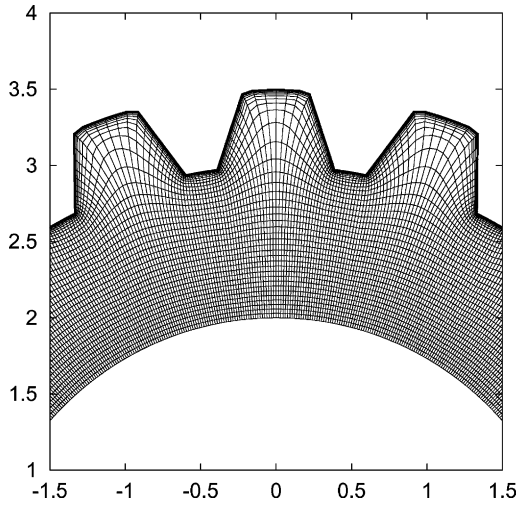

Fig. 17. Finite difference grid of a section of pinion gear, clustering parameter = 5.0.

Finally, Table 1, as shown above, characterizes the various grids generated using the new constraints. The values of the clustering parameters and the resulting averaged decay parameters corresponding to each grid are shown in this table.

5. Concluding remarks

The usefulness of the boundary constraints for elliptic grid generation problems developed in this study has been demonstrated for five internal geometrical configurations. Internal grids for an annulus, a square, a convex geometry, a gear tooth and a complete 19-tooth gear were generated using the new constraints. Smooth clustered grids have been generated using these constraints without hit-and-trial prescription of decay parameters and without any recourse to redistribution of grid points, which has been a common approach used in elliptic grid generation problems until now. With new constraints, elliptic grids can be generated in simulation time without any manual intervention thus making problems of structural dynamics and fluid dynamics over compliant boundaries more tractable. Thus, a fully automated elliptic grid generation methodology has been developed and validated.

Acknowledgements

This work was sponsered by NASA Computing, Information and Communications Technology Program.

References

[1] J.F. Thompson, F.C. Thames, C.W. Mastin, Automatic numerical generation of body-fitted curvilinear coordinate system for field containing any number of arbitrary two-dimensional bodies, J. Comput. Phys. 15 (1974) 299–319.
[2] J.F. Thompson, F.C. Thames, C.W. Mastin, TOMCAT – a code for numerical generation of boundary-fitted curvilinear coordinate systems on fields containing any number of arbitrary two-dimensional bodies, J. Comput. Phys. 24 (1977) 274–320.
[3] J.F. Thompson, AIAA J. 22 (1984) 1505.
[4] J.L. Steger, R.L. Sorenson, Automatic mesh-point clustering near a boundary in grid generation with elliptic partial differential equations, J. Comput. Phys. 33 (1979) 405–410.
[5] S.J. Alter, F.M. Cheatwood, Elliptic volume grid generation for viscous CFD parametric design studies, AIAA Paper 96-1999.
[6] Y.N. Jeng, W.J. Kuo, Two-dimensional elliptic grid solver using boundary grid control and curvature correction, AIAA J. 38 (2) (2000).
[7] U.K. Kaul, E.M. Huff, Automated gear teeth grid generation via solution of elliptic pdes, in: SIAM Conference on Geometric Design and Computing, Sacramento, CA, Nov. 5–8, 2001.
[8] U.K. Kaul, E.M. Huff, Elliptic grid generation of spiral-bevel pinion gear typical of OH-58 helicopter transmission, NASA TM-2002-210932, February 2002.
[9] U.K. Kaul, D.S. Chaussee, A comparative study of the parabolized Navier–Stokes (PNS) code using various grid generation techniques, Int. J. Comput. Fluids 13 (4) (1985) 421–441.
[10] M. Visbal, D. Knight, Generation of orthogonal and nearly orthogonal coordinates with grid control near boundaries, AIAA J. 20 (3) (1982).
[11] G. Ryskin, L.G. Leal, Orthogonal mapping, J. Comput. Phys. 50 (1983) 71–100.
[12] V. Akcelik, B. Jaramaz, O. Ghattas, Nearly orthogonal two-dimensional grid generation with aspect ratio control, J. Comput. Phys. 171 (2001) 805–821.
[13] L. Eca, 2D orthogonal grid generation with boundary point distribution control, J. Comput. Phys. 125 (1996) 440–453.